Physics and Chemistry of Minerals (2026) 53:31
https://doi.org/10.1007/s00269-026-01366-8

ORIGINAL PAPER

Capture of lanthanum atoms by the (111) twin boundary in fluorite: a DFT study

Ekaterina Y. Kotelevskaya[1] · Boris B. Shkurskii[1] · Elena A. Volkova[1] · Vasilii O. Krivchuk[2] · Daniil O. Poletaev[2] · Artem R. Oganov[2]

Received: 24 January 2026 / Accepted: 4 July 2026

Abstract
Ab initio calculations were performed to estimate the energy preference of Ca^{2+} substitution by La^{3+} with compensating incorporation of an additional F^{-} ion at the (111) twin boundary of fluorite (CaF_2). Model structures of polytypes and polysomes, which are periodic stacking faults within the cubic fluorite matrix, were constructed and optimized using density functional theory (DFT). Our results indicate that the twin boundary has a strong tendency to trap lanthanum cations. These findings suggest that the twin boundaries in CaF_2 may act as active sites for the accumulation of rare-earth elements, providing potential routes for modifying the functional properties of the materials. Conversely, addition of lanthanoids may promote growth twinning of fluorite.

Keywords Fluorite · Rare earth elements (REEs) · Twin boundary · Density functional theory (DFT) · Polytypes · Polysomes

Introduction

Calcium fluoride (CaF_2), a naturally abundant mineral fluorite, is widely used as a flux to lower melting points and remove impurities in the production of steel and aluminum, and as a key raw material for the production of hydrofluoric acid and various inorganic fluorides. Its high transparency in the UV and IR wavelengths makes it valuable in optics for the manufacture of lenses, windows and laser components. Due to their wide band gaps, many fluorides are transparent for a wide range of electromagnetic waves and are key materials for next-generation solid-state lasers (Li et al. 2024). Beyond optics, the excellent insulating properties of fluorite are being explored for applications in 2D electronics, where CaF_2 serves as a promising high-k dielectric material (Wen and Lanza 2021). In addition, fluorite is used as an additive in the ceramics and glass industries to increase stability and minimize defects. It also finds applications in specialized fields such as the nuclear industry, where it contributes to radiation resistant materials (Vasilkova and Kukushkina 1989).

Crucially, many of these advanced functionalities are not intrinsic to pristine CaF_2 but are unlocked through controlled doping and the engineering of structural defects. For instance, recent studies have demonstrated that defect-induced luminescence in REE-doped CaF_2 nanoparticles can be utilized for thermal sensing (Zhang et al. 2023), and that surface defects can dramatically enhance the material's ionic conductivity for electrochemical applications (Molaiyan and Witter 2019).

Fluorite often contains significant concentrations of rare earth elements, such as lanthanum (La), cerium (Ce) and yttrium (Y), which are highly valuable for modern industrial technologies (Vasilkova and Kukushkina 1989). These elements are critical for the production of innovative materials, as they are used in the development of high performance permanent magnets (e.g. neodymium-iron-boron, Nd-Fe-B), laser media (e.g. erbium-doped yttrium-aluminum garnets, Er: YAG), phosphors for LED lighting, and catalytic systems in petroleum refining (Li et al. 2024). The distribution of these REE dopants within the crystal is crucial, as it directly governs the material's functional properties. For

✉ Ekaterina Y. Kotelevskaya
katerina.kotelevska@mail.ru

[1] Faculty of Geology, Moscow State University, Moscow 119991, Russia

[2] Skolkovo Institute of Science and Technology, Moscow 121205, Russia

Published online: 28 August 2026

instance, the controlled segregation of REEs at grain or twin boundaries can lead to the formation of localized regions with distinct luminescent or catalytic characteristics. Therefore, understanding the fundamental mechanisms that drive REE accumulation at twin boundaries is not only of geochemical importance but also provides a potential pathway for the targeted design of advanced functional materials with enhanced properties. According to data presented in the monograph (Urusov et al. 1997), REEs indeed tend to accumulate at the grain boundaries of fluorite. This phenomenon can be explained by (i) the formation of nanoclusters containing REE atoms that are stable in defect regions of the crystal structure (Sulyanova and Sobolev 2022); (ii) the segregation of impurities in areas of structural imperfections, such as dislocations, vacancies or grain boundaries, where imperfect atomic packing creates energetically favorable conditions for the incorporation of impurity atoms (Hiraga et al. 2003). Grain boundaries, as regions of enhanced free energy, act as traps for impurities, where segregation lowers the interfacial energy and relieves local structural distortions (Priester 2013).

Segregation at ordered interfaces is also known in other classes of crystalline materials. In alloys, periodic segregation of solute atoms at fully coherent twin boundaries has been observed at the atomic scale (Nie et al. 2013). In fluorite-related oxides, the relation between grain-boundary structure and defect or solute segregation has been studied for yttria-stabilized cubic zirconia and UO_2 (Shibata et al. 2002; Symington et al. 2019). These studies provide a broader materials-science context for considering REE accumulation at ordered boundaries in fluorite.

The ability of ordered grain boundaries in fluorite to trap REEs is of particular interest. In contrast to random high-angle boundaries, these specific boundaries exhibit a periodic arrangement of atoms and high structural coherence

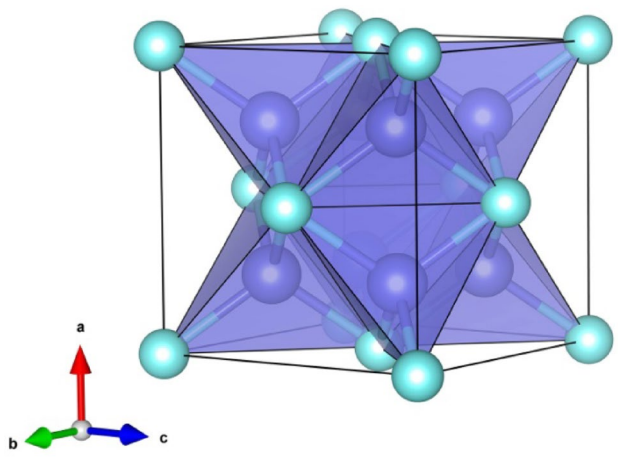

Fig. 1 Crystal structure of CaF_2 with highlighted tetrahedral interstitial sites: blue and light-blue spheres represent Ca^{2+} cations and F^- anions respectively. Visualization by VESTA (Momma and Izumi 2011)

(Warrington 1974). Twinning on {111} is a known crystallographic feature of fluorite: mineralogical descriptions report common interpenetrant twinning on {111}, and X-ray topographic studies of natural fluorite have shown that twin boundaries in interpenetrating twins can trap impurities and produce lattice distortions (Anthony et al. 2001–2005; Beswick and Lang 1972). However, the specific (111) boundary presents a notable paradox. Atomistic models predict that in pure CaF_2, the formation of the (111) twin-boundary-related h-layer is energetically unfavorable due to strong F–F electrostatic repulsion within its defect layer. At the same time, this boundary geometry is relevant for REE-bearing fluorite because of the similarity between the geometry of the cation sublattice in the defect layer and the structural motif of the aristotype of light lanthanoid trifluorides (e.g. LaF_3) (Shkurskiy 1998). Such structural similarity lowers the energy cost for substitution, creating a thermodynamically favorable site for REE incorporation. In this work, quantum-chemical modeling based on density functional theory (DFT) was employed to quantitatively investigate this stabilization mechanism by estimating the energetics of $Ca^{2+} \rightarrow La^{3+}$ substitution at the coherent (111) twin-boundary-related h-layer of CaF_2.

Crystal structures of fluorite and lanthanum trifluoride

Fluorite crystallizes in the cubic system (space group *Fm*-3*m*). Its structure consists of a face-centered cubic (*FCC*) lattice of Ca^{2+} cations in which all tetrahedral sites are occupied by F^- anions (Fig. 1). Alternatively, the structure can be viewed as a 3D chessboard made of cubes (with F^- ions at corners of the cubes) – such that cubes filled with Ca^{2+} ion and empty cubes alternate in 3D in the chessboard pattern. Each Ca^{2+} ion is surrounded by eight F^- ions in a cubic coordination (coordination number (CN_{Ca}) = 8). Each F^- ion is coordinated by four Ca^{2+} ions in a tetrahedral arrangement ($CN_F = 4$) (Sobolev 2021).

CaF_2, like many fluorite-type solids, exhibits high capacity for isomorphous substitutions and defect tolerance (Sobolev 2000). The open nature of the fluorite structure, which contains large unoccupied cubic interstitial sites combined with the flexibility of the anion sublattice (which compensates for charge imbalances during substitution), allows the substitution of Ca^{2+} by cations of similar ionic radius (e.g., Y^{3+}, La^{3+}, U^{4+}) without disrupting the structural framework. Fluorite-type structures also readily accommodate vacancies or interstitials, such as additional F^- interstitials introduced to compensate for the charge imbalance caused by the substitution of trivalent cations for Ca^{2+}.

Lanthanum and cerium trifluorides, LaF_3 and CeF_3, crystallize in the tysonite-type structure (sp. gr. $P\bar{3}c1$), which

Table 1 Comparison of CaF_2 and LaF_3 structures

Parameter	Fluorite, CaF_2	Tysonite, LaF_3
Syngony and sp. gr.	cubic, $Fm\bar{3}m$	Hexagonal, $P\bar{3}c1$
Coordination number, $^{[F]}Me$	8, cube	11, pentacapped trigonal prism
Distance *Me*-F, Å	2.38776(0)	2.73028(0)
Type of packing	Cubic close-packed, *FCC*	Hexagonal close-packed, *HCP*

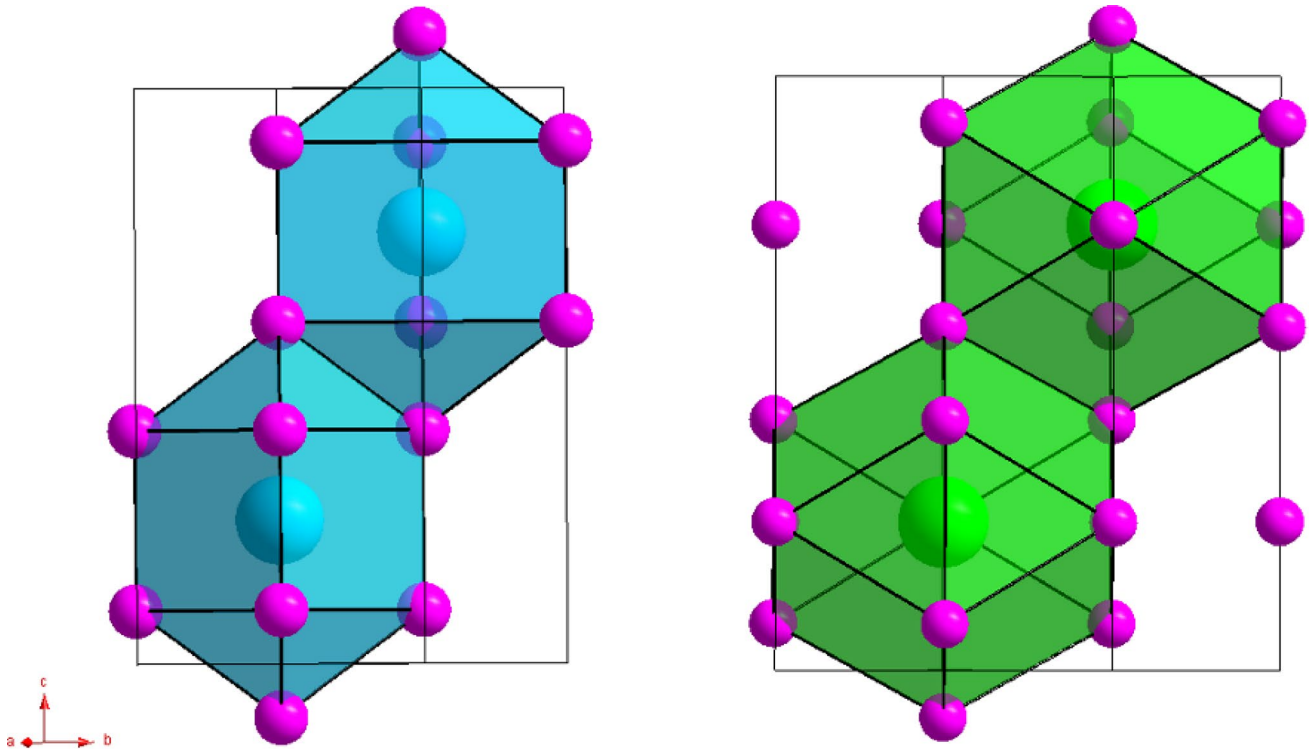

Fig. 2 Crystal structures of the hexagonal CaF_2 polytype (left) and hexagonal LaF_3 (tysonite structure, right). The larger central spheres represent cations (Ca^{2+} and La^{3+}) and the smaller spheres represent fluoride (F^-) anions. Visualization by Diamond (Crystal Impact 2023)

is characteristic of light lanthanoids with large ionic radii (Sobolev et al. 2016). A key feature of this aristotype structure is that the Ln^{3+} cations form a hexagonal close packing (HCP) arrangement. The F^- anions occupy interstitial sites such that each La^{3+} cation is coordinated by 11 fluorine atoms. This coordination polyhedron is described as a pentacapped trigonal prism, consisting of 6 anions at the prism vertices and 5 capping anions located in the equatorial and axial positions (Sobolev 2021).

Both structure types, CaF_2 and LaF_3 can be described within the language of close packings, which explains the formation of coherent twin boundaries and syntactic (oriented) intergrowths in the CaF_2-LaF_3 system. The structural relationship between the hexagonal LaF_3 (tysonite) and the hexagonal representation of the CaF_2 structure (the 2 H polytype, CaF_2_Hex) is illustrated in Table 1; Fig. 2.

Coherent twin boundaries arise when two twinned crystals share a boundary plane with a high degree of lattice matching. Syntactic, or oriented, intergrowth refers to the ordered overlay of the crystal structure of one grain on the other while maintaining orientation coherence.

The twin boundary along the (111) plane in CaF_2 is a special type of intergranular boundary known as a coincidence site lattice (*CSL*) with a parameter $\Sigma=3$. The *CSL* model describes the coincidence of lattice nodes between two interpenetrating crystals at a specific misorientation angle. The parameter Σ describes the geometric compatibility of the lattices, representing the inverse density of coinciding nodes. A smaller Σ value corresponds to a higher density of matching nodes and often lower boundary energy (Randle 2001). At this boundary, the crystal lattice undergoes mirror reflection relative to the (111) plane. Within the cation sublattice, this creates a stacking fault, forming a single layer with a local HCP stacking sequence, (hereafter referred to as the ***h*-layer**), which is embedded within the bulk crystal matrix that retains its normal FCC stacking (hereafter referred to as ***c*-layers**).

Since coherent twin boundaries in FCC crystals act as intrinsic stacking faults with local HCP symmetry, they

create a specific structural niche within the cubic matrix. Given that the cation sublattice of LaF_3 is also HCP-based, the twin boundary in CaF_2 effectively recreates the coordination environment preferred by lanthanum, thereby promoting its segregation.

In this *h*-layer, the local HCP stacking sequence forces the anion-centered coordination tetrahedra (FCa_4) to share faces, in contrast to the edge-sharing arrangement in the bulk fluorite structure. (Sobolev 2021). The modified coordination of Ca^{2+} in the *h*-layer can influence the boundary's properties, including its ability to concentrate impurities. In this layer, F^-centered FCa_4-tetrahedra connect *via* shared faces. This leads to strong electrostatic repulsion between closely spaced F^- anions in adjacent tetrahedra, resulting in the destabilization of the structure. Replacing Ca^{2+} with La^{3+} in the *h* layer requires charge compensation by the incorporation of additional F^- ions, which occupy trigonal interstitial sites within the *h* layer. This increases the coordination number of La^{3+} to 11, forming a penta-capped trigonal prism (Fig. 3) - a coordination environment analogous to that found in lanthanoid trifluorides (e.g., LaF_3). While the F^--F^- repulsion still exists, it is effectively overcome by the much stronger La^{3+}-F^- electrostatic attraction, leading to a net stabilization of the layer.

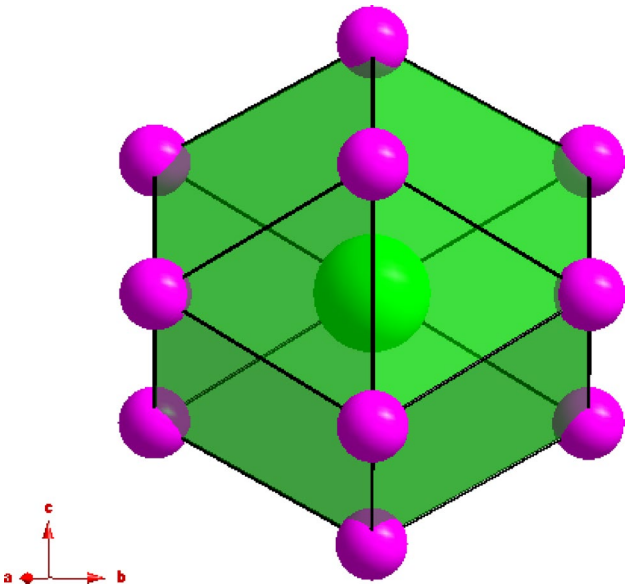

Fig. 3 Penta-capped trigonal prism, representing the coordination polyhedron of the La^{3+} cation in the tysonite (LaF_3) structure. This 11-fold coordination environment is also adopted by lanthanum atoms at the (111) twin boundary. The central sphere is the La^{3+} cation, surrounded by 11 F^- anions. Visualization by Diamond (Crystal Impact 2023)

Computational methods

Density functional theory (DFT) was used as the main quantum-chemical method for calculating the total energies and optimized atomic structures of the model systems. DFT is one of the standard approaches in computational materials science, where the total energy of an electronic system is treated as a functional of the electron density. In the Kohn–Sham formulation, the interacting many-electron problem is replaced by an auxiliary system of non-interacting electrons moving in an effective potential (Hohenberg and Kohn 1964; Kohn and Sham 1965). This approach makes it possible to calculate equilibrium structures, relative energies and defect-related structural changes in crystals from first principles.

All calculations were performed using the Vienna Ab initio Simulation Package (VASP) (Kresse and Hafner 1993; Kresse and Furthmüller 1996a, b). The exchange–correlation energy was described within the generalized gradient approximation using the Perdew–Burke–Ernzerhof functional (Perdew et al. 1996). Electron–ion interactions were treated using the projector augmented-wave method (Blöchl 1994; Kresse and Joubert 1999). The PAW datasets included 11 valence electrons for La, 10 for Ca and 7 for F.

A plane-wave cutoff energy of 520 eV was used for all models. This value was chosen to provide a sufficiently accurate plane-wave basis for the considered Ca–F and La–F structures while keeping the calculations feasible for the largest supercells. The Brillouin zone was sampled using automatically generated k-point meshes with KSPACING = 0.15 $Å^{-1}$. This setting was used to keep a comparable k-point density for cells of different sizes along the [111] stacking direction.

Electronic self-consistency was reached using an energy convergence criterion of 10^{-4} eV. This criterion was used as a stable threshold for structural optimization of the relatively large periodic models. To improve the stability of the self-consistent-field procedure for the ionic supercells, the charge-density mixing parameters were set to AMIX = 0.01 and AMIN = 0.01. In addition, NELMDL = 6 was used to introduce an initial delay in the electronic relaxation, which helps stabilize the first electronic steps when the initial charge density and orbitals are still far from self-consistency.

Structural optimization was performed in two steps. First, the model structures were relaxed using the conjugate-gradient algorithm (IBRION = 2), which was used as a robust initial relaxation scheme for structures that may be relatively far from equilibrium. A Methfessel–Paxton smearing scheme of first order was used during this preliminary stage (ISMEAR = 1, SIGMA = 0.10 eV) to improve numerical stability during relaxation.

After reaching the vicinity of the local minimum, an additional refinement relaxation was performed using the quasi-Newton algorithm (IBRION = 1), which is efficient for structures already close to equilibrium. In this final refinement step, Gaussian smearing was used (ISMEAR = 0, SIGMA = 0.10 eV), which is more appropriate for insulating CaF_2-based structures. The resulting refined structures and total energies were used for the energetic analysis discussed below.

In all relaxation steps, atomic positions, cell shape and cell volume were allowed to relax, corresponding to ISIF = 3. This setting was used because the introduction of h-layers and La–F structural fragments can affect both internal coordinates and lattice parameters. The maximum number of ionic steps was set to NSW = 500 to allow convergence of the largest models. A small step-size scaling factor, POTIM = 0.02, was used to avoid excessively large ionic displacements during optimization. The relaxation was stopped when the forces became smaller than 0.001 $eV \cdot Å^{-1}$, corresponding to EDIFFG = -10^{-3} $eV \cdot Å^{-1}$.

Two series of periodic model structures were considered: pure Ca–F polytypes and La-containing polysomes. The construction of these models, the definition of the dilution parameter x, and the geometrical parameters of the cells are described in the next section. The cell size along the [111] stacking direction was systematically varied to separate neighboring h-layers and to extrapolate the excess energies to the dilute limit.

Design of model structures

The model construction was aimed at testing a specific coherent (111) twin-boundary-related h-layer motif in the CaF_2–LaF_3 system. Because a grain boundary is not fully specified by the Sigma value alone (Randle 2001), both the boundary plane and the local stacking geometry were fixed explicitly in the model. The calculated energies discussed below therefore refer to this selected coherent h-layer geometry.

Two related series of periodic model structures were constructed (Fig. 4). The first series consists of pure Ca–F polytypes and represents the (111) h-layer motif in pure CaF_2. The second series consists of La-containing polysomes and represents the same h-layer motif after $Ca^{2+} \rightarrow La^{3+}$ substitution with compensating incorporation of additional F^- ions (Aksenov et al. 2023). The use of two parallel series allows the energetic effect of La incorporation to be separated from the intrinsic energy cost of the pure h-layer.

The starting point for both series was a hexagonal representation of the fluorite structure along the [111] direction. In this description, the cation sublattice is treated as a close-packed sequence of Ca^{2+} layers. The normal cubic fluorite blocks preserve the ABCABC… stacking sequence and are denoted below as c-layers. A local reversal of the stacking sequence, written schematically as …ABC|CBA…, produces a mirror-related h-layer associated with the coherent (111) twin-boundary motif.

This stacking construction follows the crystal-chemical model proposed by Shkurskiy (1998) for REE-bearing fluorite. In that model, the atomic arrangement near a (111)-type twin boundary is described by the (…A, BCB, A…) sequence obtained from the cubic (…ABCABC…) fluorite sequence by reflection. The selected geometry is also consistent with interface-model generation for fluorite-structure compounds, where the Sigma 3 (111)/(11$\bar{1}$) interface was found to have a restricted set of in-plane rigid-body translations (Hinuma 2022). In the present work, the in-plane translation was therefore not treated as an independent variable; the calculations were focused on the mirror-related h-layer geometry defined above.

In the pure polytype series, only Ca and F atoms were included. Fluoride ions were placed in tetrahedral interstices of the close-packed cation sublattice, as in the fluorite structure. In the h-layer, this construction leads to face-sharing FCa_4 tetrahedra and short F–F contacts. The pure polytype series was therefore used as a reference for estimating the energy cost associated with introducing the h-layer into the CaF_2 matrix.

The La-containing polysome series was constructed from the same stacking sequence. In the h-layer, Ca^{2+} cations were replaced by La^{3+}, and additional F^- ions were introduced near the h-layer to compensate the heterovalent substitution. This choice follows the fluorine-rich $M_{1-x}R_xF_{2+x}$ description of REE-bearing fluorite-type phases and allows the local coordination environment to approach the LaF_3-like motif discussed in the previous sections. Alternative charge-compensation mechanisms, including Ca vacancies, are considered in the Discussion.

The model notation 1_C is used for a periodic structure containing one h-layer and C cubic c-layers per repeat unit. For these models, the dilution parameter x is defined as the fraction of h-layers in the stacking sequence, x = H/(H + C), where H = 1 for the series considered here. Increasing C therefore decreases x and separates neighboring h-layers by thicker cubic CaF_2 blocks. Representative members of the series, including the 1_3 and 1_9 models, are shown in Fig. 4.

The cell height along [111] was varied systematically to reduce the interaction between periodically repeated h-layers. The dilute-limit excess energy was then estimated by extrapolating the calculated energies as a function of x. This approach avoids assigning the energy of the boundary from a single finite cell and instead uses the trend obtained from the whole dilution series.

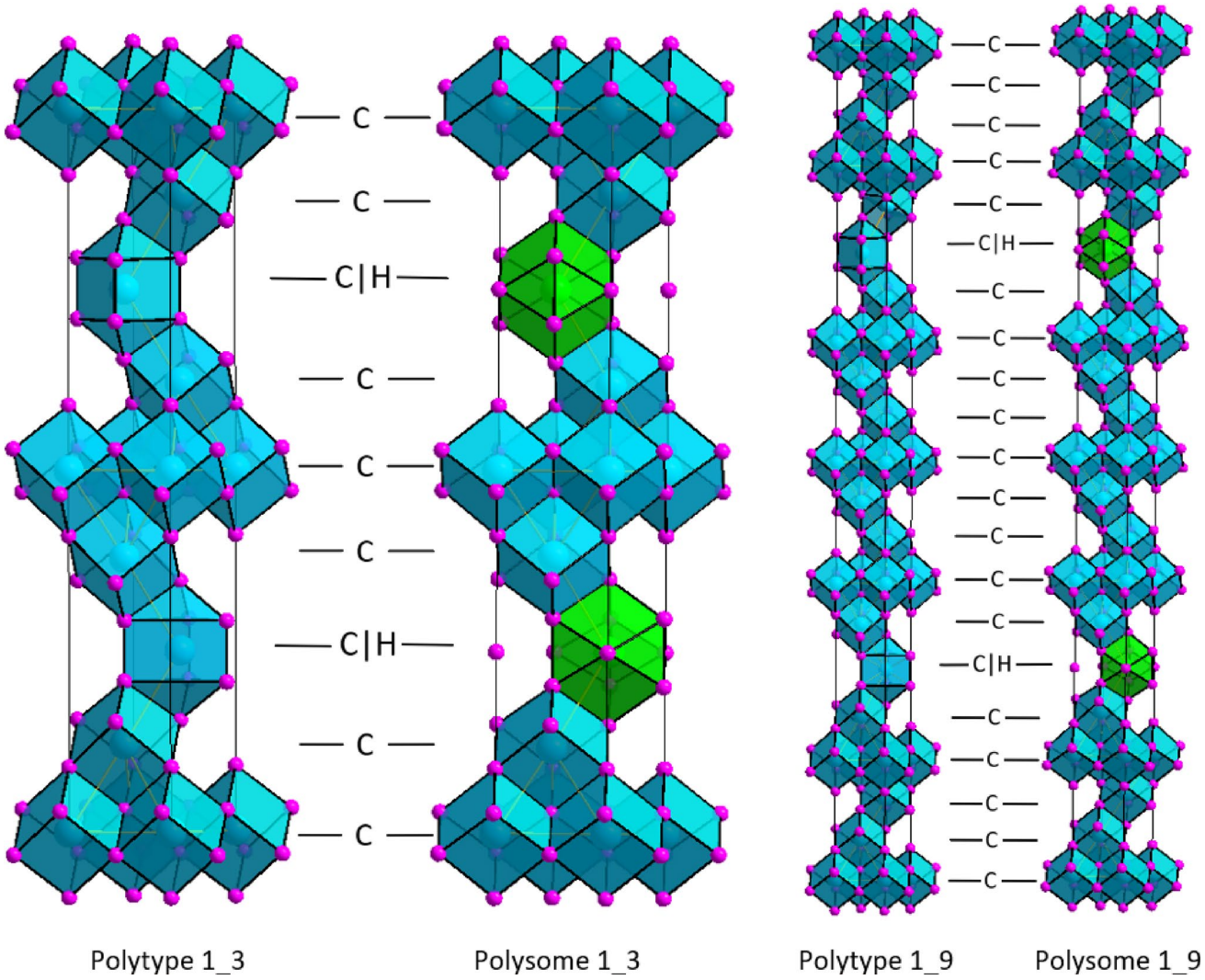

Fig. 4 Model structures employed in our calculations: blue, violet and green spheres represent Ca^{2+}, F^- and La^{3+} ions respectively. Structures shown are intermediate members (e.g., polytype 1_3 with C = 3 cubic layers and H = 1 hexagonal layer per lattice period) that illustrate the progressive dilution of the hexagonal defect layers within the cubic fluorite matrix. Visualization by Diamond (Crystal Impact 2023)

Table 2 Representative model parameters used for the dilution series

Model	H	C	x = H/(H + C)	C_h, Å	Structural meaning
1_1	1	1	0.50	6.34	High density of h-layers
1_3	1	3	0.25	12.68	Intermediate model shown in Fig. 4
1_5	1	5	0.1667	19.02	Intermediate dilution
1_7	1	7	0.125	25.36	Intermediate dilution
1_9	1	9	0.1	31.70	Diluted model shown in Fig. 4
1_11	1	11	0.0833	38.04	Most diluted model in the series

In all models, the lateral parameters of the hexagonal cell in the boundary plane were derived from the optimized cubic fluorite parameter as $a_h = b_h = a_c/\sqrt{2}$. With $a_c \approx 5.49$ Å, this gives $a_h = b_h \approx 3.88$Å. The cell height C_h along the [111] stacking direction was varied by changing the number of cubic c-layers between neighboring h-layers. Model parameters are presented in Table 2.

The initial structures generated from ideal close-packing rules contained very short F–F contacts in the h-layer. Such contacts are expected from the face-sharing arrangement of FCa_4 tetrahedra, but they can also make the first steps of geometry optimization unstable. Therefore, before DFT relaxation, only the starting geometries were adjusted by slightly changing the initial layer spacing and by placing F^- ions near the centers of their coordination polyhedra. These adjustments were used only to prepare physically reasonable starting configurations. All final structures and energies were obtained after full DFT relaxation.

The relaxed structures obtained from these two series were used for the energy analysis in the following section.

Crystal-chemical potential

To quantitatively assess the energetic favorability of $Ca^{2+} \rightarrow La^{3+}$ substitution at the (111) twin boundary in fluorite, we introduce the crystal-chemical potential, a quantity characterizing the energy change in the crystal due to atomic substitution. Similar to the chemical potential of a component in solutions, it determines the thermodynamic tendency of cations to redistribute between phases or lattice sites (Wood and Fraser 1977). In this work, μ* is used as a model-dependent excess-energy parameter obtained from the dilute-limit extrapolation. The calculated crystal-chemical potential reflects the cumulative impact of several key physical effects arising from the substitution. These effects include:

1. Deformations caused by the difference in ionic radii between Ca^{2+} and La^{3+}, and the resulting changes in interatomic distances near the substituted cation.
2. The restructuring of the cation's coordination polyhedron from an 8-fold cube (CaF_8) to an 11-fold pentacapped trigonal prism (LaF_{11}), which alters the geometry of the coordination polyhedra and the distances between anions.
3. The necessity of charge compensation via an additional F^- anion during the $Ca^{2+} \rightarrow La^{3+}$ substitution, along with the subsequent redistribution of electron density at the boundary region.
4. The influence of ionic size on the local packing density and the potential formation of strained regions at the substitution sites.

As direct DFT calculations for systems with a large number of cubic layers (C) are computationally prohibitive, we used an analytical approach to determine the energy of an isolated twin boundary. We calculated the total energy E for a series of structures with varying defect concentrations ($x = 1/(C+1)$) and then extrapolated these results to the limit of infinite dilution ($x \rightarrow 0$).

This extrapolation relies on the concept of a "crystal-chemical potential" (μ*), which is formally defined as the derivative of the system's energy with respect to the defect concentration in the limit of infinite dilution:

$$\mu^* = \frac{dE}{dx} \, as \, x \rightarrow 0$$

In practice, this value is determined by fitting a polynomial function to the calculated data points and finding the slope of the tangent to the curve at $x = 0$.

Analogous to the chemical potential of a component in a solution, the crystal-chemical potential μ* represents the energy change associated with introducing a single defect layer into the pure, defect-free crystal matrix. Therefore, its sign provides insight into the stability of the boundary: a positive value indicates an energy cost for defect formation, making the process unfavorable, while a negative value signifies that defect formation is energetically favorable.

Table 3 Energies of model structures relative to pure CaF_2

x	Polytype energy, eV	Polysome energy, eV
0	0	0
0.0833	0.1173	−0.7351
0.1	0.1349	−0.8756
0.125	0.1670	−1.1251
0.1667	0.2163	−1.5209
0.25	0.3178	−2.2785
0.5	0.6129	−4.6457
1	1.1100	−9.5517

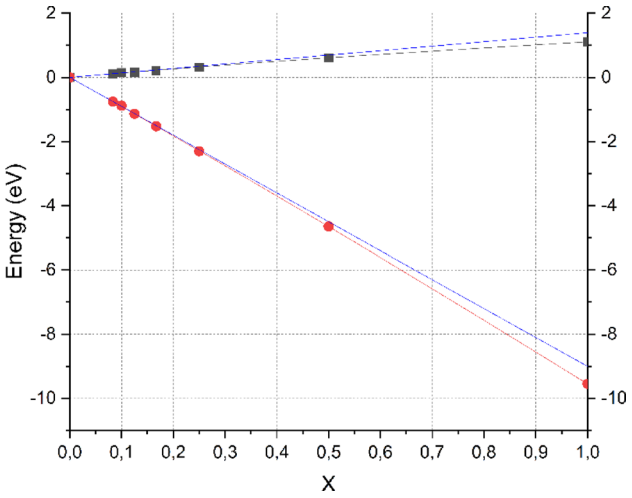

Fig. 5 Partial energy (referenced to pristine fluorite) as a function of composition. Black squares represent the calculated energies for the series of polytypes (pure CaF_2), while the red circles show the energies for the series of polysoms (La-doped). Solid lines represent the fitted polynomials. The blue lines indicate tangents to these curves at $x = 0$

Results

The DFT-calculated energies for the polytype and polysome series, referenced to the energy of bulk CaF_2, are presented in Table 3 and plotted as a function of defect concentration x in Fig. 5. By fitting these data and extrapolating to $x \rightarrow 0$, we determined the crystal-chemical potentials (μ*) for incorporating a pure hexagonal layer and a La-doped hexagonal layer into the CaF_2 matrix. The potentials were found to be:

$$\mu^* \left(CaF_2^{def} \right) = +1.3\,(9) \text{ eV}$$

$$\mu^{*}\left(\mathrm{LaF}_3^{def}\right) = -9.0\,(0)\ \mathrm{eV}$$

The positive value for the pure CaF_2 defect indicates that forming the twin boundary is energetically costly. Conversely, the large negative value for the La-doped defect shows a strong thermodynamic driving force for its formation.

To quantify the overall energy gain from substituting Ca with La at the boundary, we considered the following reaction:

$$\mathrm{CaF}_2^{def} + \mathrm{LaF}_3^{hex} \rightarrow \mathrm{LaF}_3^{def} + \mathrm{CaF}_2^{cub}$$

This reaction describes the process where a hexagonal LaF_3 unit $\left(\mathrm{LaF}_3^{\mathrm{hex}}\right)$ replaces a hexagonal CaF_2 unit at the defect boundary ($\mathrm{CaF}_2^{\mathrm{def}}$), effectively transforming the defect layer from pure to La-doped.

The energy change for this reaction (ΔE_{subst}) can be calculated from the determined crystal-chemical potentials and the total energy of the hexagonal LaF_3 bulk structure. The energy of the defect layers is given by their potentials (μ*), while the energy of the bulk structures is taken relative to CaF_2^{cub} (E=0). The DFT-calculated energy for bulk hexagonal LaF_3 (LaF_3^{hex}) is −9.552 eV.

Thus, the substitution energy is:

$$\Delta E_{mol} = [E\left(\mathrm{LaF}_3^{def}\right) + E\left(\mathrm{CaF}_2^{cub}\right)] - [E\left(\mathrm{CaF}_2^{def}\right) + E\left(\mathrm{LaF}_3^{hex}\right)]$$

Considering the normalization of energies to CaF_2 energy (where $E\left(\mathrm{CaF}_2^{cub}\right) = 0$):

$$\Delta E_{mol} = [\mu^{*}\left(\mathrm{LaF}_3^{def}\right) + 0] - [\mu^{*}\left(\mathrm{CaF}_2^{def}\right) + E\left(\mathrm{LaF}_3^{hex}\right)]$$

$$\Delta E_{mol} = [-9.0(0)] - [+1.3(9) + (-9.55)] \approx -0.84\,eV$$

The resulting negative energy of **−0.8(4) eV** indicates that the substitution of Ca by La at the (111) twin boundary is a strongly exothermic and thus highly favorable process.

Thermodynamic stability analysis

To rigorously evaluate the stability of the twin boundary in an open system where the local chemical composition can vary, we employed the thermodynamic formalism of the grand canonical ensemble. This approach, widely used for predicting surface and interface reconstructions with variable stoichiometry (Zhu et al. 2013), allows us to determine the lowest-energy structure as a function of the chemical potential of the dopant.

The stability of a grain boundary supercell is determined by the grand canonical potential (Gibbs free energy of formation), Ω, defined as:

$$\Omega = \frac{1}{2A}\left(E_{total} - \sum\nolimits_1 N_i\mu_i\right)$$

where E_{total} is the total DFT energy of the supercell, N_i is the number of atoms of species i (Ca, F, La), and μ_i is the atomic chemical potential.

Since the bulk matrix remains pure fluorite, the chemical potentials of calcium and fluorine are constrained by the equilibrium with bulk CaF_2 ($\mu_{Ca} + 2\mu_F = E^{bulk}_{CaF_2}$). The lanthanum dopant is assumed to be in equilibrium with a reservoir of LaF_3, such that its chemical potential can be expressed relative to the bulk LaF_3 phase:

$$\mu_{La} = E^{bulk}_{LaF_3} - 3\mu_F + \Delta\mu_{LaF_3}$$

Here, $\Delta\mu_{LaF_3}$ serves as the thermodynamic variable representing the availability of lanthanum in the environment, ranging from the precipitation limit ($\Delta\mu = 0$) to dilute solid solutions ($\Delta\mu < 0$).

Substituting these constraints into equation for Ω and considering the stoichiometric substitution mechanism ($Ca^{2+} \rightarrow La^{3+} + F^{-}$), the formation energy relative to the pure fluorite boundary can be expressed as:

$$\Omega\left(\Delta\mu_{LaF_3}\right) = E_{rel} - x\cdot\left(E^{bulk}_{LaF_3} + \Delta\mu_{LaF_3}\right)$$

Here, x is the dilution parameter ($x = 1/(C+1)$), representing the fraction of hexagonal stacking faults in the fluorite matrix. For the **polysome** series, where the hexagonal layers act as segregation sites composed of LaF_3 structural units, the parameter x also corresponds to the molar fraction of lanthanum in the supercell. The term $\Delta\mu_{LaF_3}$ represents the chemical potential of LaF_3 relative to its bulk phase, ranging from the precipitation limit ($\Delta\mu = 0$) to dilute solid solutions ($\Delta\mu < 0$). $E_{rel}(x)$ is the DFT-calculated energy of the supercell relative to pure bulk CaF_2 (Table 3).

Figure 6 illustrates the calculated stability diagram. The plot reveals a competition between the formation of pure stacking faults (polytypes, horizontal dashed lines) and La-segregated boundaries (polysomes, solid sloped lines).

The formation energy of the pure twin boundary structures (dashed lines) is positive and independent of the La chemical potential. For the highest defect density ($x = 0.5$), this cost is approximately +0.61 eV per formula unit, confirming that the formation of the considered h-layer motif is energetically unfavorable.

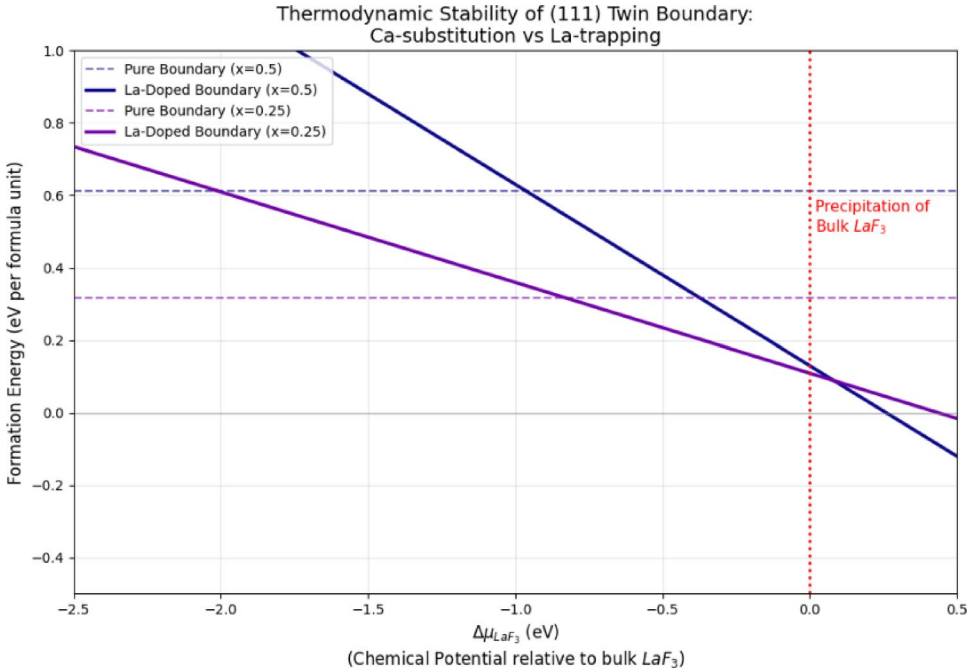

Fig. 6 Thermodynamic stability of the (111) twin boundary phases as a function of the chemical potential of LaF_3. Horizontal dashed lines represent the formation energy of pure boundaries (Polytypes). Solid sloped lines represent the grand potential of La-doped boundaries (Polysomes)

The solid lines, representing the La-doped phases, show a negative slope, indicating that increasing the availability of La stabilizes the structure. A crossover occurs at $\Delta\mu \approx -1.0$ eV. At chemical potentials higher than this value (closer to zero), the La-doped structures become lower in energy than their pure counterparts, signifying that *lanthanum trapping becomes thermodynamically favorable*. Near the saturation limit ($\Delta\mu \approx 0$), the La-doped phase with $x = 0.5$ exhibits an energy of $\approx +0.13$ eV, which is significantly lower than the energy of the corresponding pure polytype ($\approx +0.61$ eV). This energy difference ($\Delta\Omega \approx -0.48$ eV per formula unit) represents the total thermodynamic gain of the supercell. When normalized by the lanthanum concentration ($x = 0.5$), this corresponds to a stabilization energy of roughly *−0.96 eV per substituted La cation*. This value is consistent with the substitution energy of −0.8(4) eV calculated via the analytical method in the Results section, confirming a strong driving force for segregation.

To compare the excess energy of the pure h-layer with conventional interface energies, the dilute-limit parameter μ* was converted into an energy per unit area. In the present normalization, μ* corresponds to one h-layer structural unit. The area of this unit in the (111) plane was estimated from the hexagonal in-plane parameter a_h. For the cubic fluorite cell, $a_h = a_c/\sqrt{2}$; using the optimized value $a_c \approx 5.49$Å gives $a_h \approx 3.88$ Å. The corresponding area is $A(111) = (\sqrt{3}/2)\, a_h^2 \approx 13.0\ \text{Å}^2$. Thus, the value μ* ≈ 1.35–1.39 eV obtained for the pure Ca–F series corresponds to $\gamma_h \approx 0.104 - 0.107\ eV \cdot \text{Å}^{-2}$, or approximately $1.66 - 1.71\ J \cdot m^2$. This value refers to the coherent mirror-related h-layer motif considered in this work and should not be interpreted as a globally optimized energy of all possible Σ3{111} boundary configurations.

The local atomic structures after full DFT relaxation are shown in Fig. 7. In the pure Ca–F model, the selected F–F distance near the h-layer is 2.26 Å. In the La-containing model, the corresponding selected F–F distance increases to 2.48 Å. Both distances are shorter than the nearest-neighbour F–F separation expected for ideal cubic CaF_2, which is approximately a_c/2≈2.75 Å for the optimized lattice parameter used here. This comparison shows that the pure h-layer retains a more compressed anion arrangement after relaxation. In the La-containing model, the additional F^- anion is incorporated into the local La–F coordination environment, producing a fluorine-rich fragment related to tysonite-type LaF_3. This structural change is consistent with the lower excess energy of the La-containing polysome series.

Discussion and conclusions

The calculated energies support the crystal-chemical hypothesis that La incorporation can stabilize the coherent (111) twin-boundary-related h-layer motif in fluorite. In the pure CaF_2 model, formation of the h-layer is energetically costly, as reflected by the positive crystal-chemical potential of the pure Ca–F series. In contrast, the La-containing polysome series gives a negative excess-energy contribution within the same reference scheme. Thus, the energetic

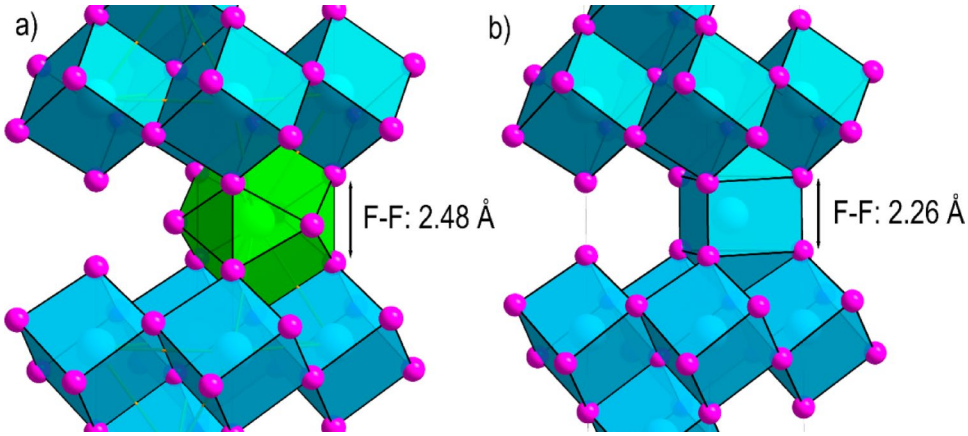

Fig. 7 Local atomic structures of the h-layer region after full DFT relaxation: **a** La-containing h-layer with charge compensation by an additional F^- anion and **b** pure Ca–F h-layer. blue, violet and green spheres represent Ca^{2+}, F^- and La^{3+} ions respectively. The selected F–F distances near the h-layer are shown. Visualization by Diamond (Crystal Impact 2023)

result should be interpreted as stabilization of the considered fluorine-rich LaF_3-like h-layer motif, rather than as a general statement about all possible Σ3{111} grain-boundary structures in CaF_2.

The difference between the pure and La-containing models is consistent with the relaxed local structures. In the pure Ca–F model, the h-layer preserves a compressed fluorite-related anion arrangement after relaxation. In the La-containing model, the additional F^- anion is incorporated into the local La–F coordination environment, producing a fluorine-rich fragment related to tysonite-type LaF_3. Therefore, the stabilization is not only associated with the replacement of Ca^{2+} by the larger La^{3+} cation, but also with the formation of a local coordination environment that is more suitable for La in a fluorine-rich structure.

The calculated h-layer energy should be understood with respect to the model construction used in this work. The present calculations do not represent an exhaustive search over all possible rigid-body translations, reconstructions, or alternative atomic densities of a Σ3{111} boundary. Instead, they test a specific mirror-related h-layer geometry derived from the crystal-chemical model of REE-bearing fluorite. This distinction is important because the atomic structure and energy of grain boundaries are not determined by the Σ value alone; they also depend on the boundary plane and the local interfacial geometry.

The charge-compensation mechanism considered here is also model-specific. In the polysome series, $Ca^{2+} \rightarrow La^{3+}$ substitution is compensated by additional F^- anions. This choice follows the fluorine-rich $M_{1-x}R_xF_{2+x}$ trend known for REE-bearing fluorite-type nonstoichiometric phases and is required for the formation of the LaF_3-like local boundary fragment considered in this work. The preference for interstitial-F^- compensation is also consistent with the defect chemistry of bulk CaF_2. In fluorite, anion Frenkel disorder is considerably less costly than cation-sublattice disorder: reported formation energies are 2.6–2.7 eV for anion Frenkel pairs and 8.5–9.2 eV (Catlow and Norgett 1973) for cation Frenkel pairs. Interstitial fluoride ions are also known as charge-compensating defects for trivalent rare-earth dopants in CaF_2 (Huisinga 1998). Therefore, although Ca-vacancy compensation cannot be excluded under other chemical-potential conditions, the interstitial-F^- mechanism used here is the more natural choice for constructing a fluorine-rich LaF_3-like boundary fragment. Calcium-vacancy compensation is possible in principle under different chemical-potential conditions. However, such a mechanism would produce a cation-deficient boundary environment rather than the fluorine-rich La–F coordination motif studied here. A direct comparison between interstitial-F^- and Ca-vacancy compensation would require additional defect models and a separate chemical-potential analysis.

The polysome models used in this work should be regarded as ordered periodic approximants to La-enriched h-layers. They do not sample all possible dilute, partially occupied, or laterally disordered La configurations along an extended boundary. In natural fluorite, several REE species may also be present simultaneously, and their distribution may depend on ionic radius, local boundary structure and the charge-compensation mechanism. The present calculations were performed for La as a representative large trivalent cation and do not resolve competitive segregation between different REEs. Testing these effects would require larger lateral supercells and additional calculations for different REE species and defect configurations.

The results are consistent with reports that REEs tend to accumulate at grain boundaries in fluorite and with the crystal-chemical model in which REE-bearing, tysonite-like fragments may be associated with twin-boundary-related defects. At the same time, the present work does not claim direct experimental observation of the exact La-decorated atomic structure studied here. Rather, it provides a DFT-based energetic test of a crystallographically and crystal-chemically motivated mechanism for La stabilization at the coherent (111) h-layer motif.

In summary, the calculations indicate that La incorporation together with additional F^- can reduce the energetic cost of forming the considered coherent h-layer in CaF_2. This provides a possible atomistic mechanism for REE enrichment at twin-boundary-related defects in fluorite and motivates further experimental studies of REE distributions at fluorite twin boundaries.

Author contributions The manuscript was written through contributions of all authors. All authors have given approval to the final version of the manuscript. All authors contributed equally.

Funding This work was supported by the Russian Science Foundation (grant No. 24-43-00162). Calculations were performed on the Oleg supercomputer of the Materials Discovery Laboratory at Skoltech.

Data availability The structural models and datasets generated during the current study are available from the corresponding author on reasonable request.

Code Availability The calculations were performed using the VASP software package. Visualization and structural analysis were performed using VESTA and Diamond software.

Declarations

Conflict of interest The authors have no relevant financial or non-financial interests to disclose.

Ethical approval Not applicable.

Consent to participate Not applicable.

Consent for publication Not applicable.

References

Aksenov SM et al (2023) Modularity, polytypism, topology, and complexity of crystal structures of inorganic compounds. J Struct Chem 64(10):1797–2028. https://doi.org/10.1134/S0022476623100013

Anthony JW, Bideaux RA, Bladh KW, Nichols MC (eds) (2001–2005) Fluorite CaF_2. Handbook of Mineralogy. Mineral Data Publishing, Tucson. https://www.handbookofmineralogy.org/pdfs/fluorite.pdf

Beswick DM, Lang AR (1972) Some X-ray topographic observations on natural fluorite. Philos Mag 26(5):1057–1070. https://doi.org/10.1080/14786437208227363

Blöchl PE (1994) Projector augmented-wave method. Phys Rev B 50(24):17953–17979. https://doi.org/10.1103/PhysRevB.50.17953

Catlow CRA, Norgett MJ (1973) Shell model calculations of the energies of formation of point defects in alkaline earth fluorides. J Phys C: Solid State Phys 6(8):1325–1339. https://doi.org/10.1088/0022-3719/6/8/002

Crystal I (2023) Diamond – Crystal and Molecular Structure Visualization. Dr H Putz & K Brandenburg GbR, Bonn, Germany https://www.crystalimpact.de/diamond

Hinuma Y (2022) Modeling interfaces of fluorite-structure compounds using slab charge distribution. Sci Technol Adv Mater Methods 2(1):392–401. https://doi.org/10.1080/27660400.2022.2126739

Hiraga T, Anderson IM, Kohlstedt DL (2003) Chemistry of grain boundaries in mantle rocks. Am Mineral 88(7):1015–1019. https://doi.org/10.2138/am-2003-0709

Hohenberg P, Kohn W (1964) Inhomogeneous electron gas. Phys Rev 136(3B):B864–B871. https://doi.org/10.1103/PhysRev.136.B864

Huisinga M (1998) Ultraviolet photoelectron spectroscopy and electron stimulated desorption from CaF_2. PhD thesis, Freie Universität Berlin

Kohn W, Sham LJ (1965) Self-consistent equations including exchange and correlation effects. Phys Rev 140(4A):A1133–A1138. https://doi.org/10.1103/PhysRev.140.A1133

Kresse G, Furthmüller J (1996a) Efficiency of ab-initio total energy calculations for metals and semiconductors using a plane-wave basis set. Comput Mater Sci 6(1):15–50. https://doi.org/10.1016/0927-0256(96)00008-0

Kresse G, Furthmüller J (1996b) Efficient iterative schemes for ab initio total-energy calculations using a plane-wave basis set. Phys Rev B 54(16):11169–11186. https://doi.org/10.1103/PhysRevB.54.11169

Kresse G, Hafner J (1993) Ab initio molecular dynamics for liquid metals. Phys Rev B 47(1):558–563. https://doi.org/10.1103/PhysRevB.47.558

Kresse G, Joubert D (1999) From ultrasoft pseudopotentials to the projector augmented-wave method. Phys Rev B 59(3):1758–1775. https://doi.org/10.1103/PhysRevB.59.1758

Li X et al (2024) Fluoride transparent ceramics for solid-state lasers: A review. J Adv Ceram 13(12):1891–1918. https://doi.org/10.26599/JAC.2024.9220986

Molaiyan P, Witter R (2019) Surface defect-enhanced conductivity of calcium fluoride for electrochemical applications. Mater Des Process Commun 1(5):e90. https://doi.org/10.1002/mdp2.44

Momma K, Izumi F (2011) VESTA 3 for three-dimensional visualization of crystal, volumetric and morphology data. J Appl Crystallogr 44:1272–1276. https://doi.org/10.1107/S0021889811038970

Nie JF, Zhu YM, Liu JZ, Fang XY (2013) Periodic segregation of solute atoms in fully coherent twin boundaries. Science 340(6135):957–960. https://doi.org/10.1126/science.1229369

Perdew JP, Burke K, Ernzerhof M (1996) Generalized gradient approximation made simple. Phys Rev Lett 77(18):3865–3868. https://doi.org/10.1103/PhysRevLett.77.3865

Priester L (2013) Grain Boundaries: From Theory to Engineering. Springer, Berlin Heidelberg. https://doi.org/10.1007/978-94-007-4969-6

Randle V (2001) The coincidence site lattice and the 'sigma enigma'. Mater Charact 47(6):411–416. https://doi.org/10.1016/S1044-5803(02)00193-6

Shibata N, Oba F, Yamamoto T, Ikuhara Y, Sakuma T (2002) Atomic structure and solute segregation of a Σ=3, [110]/{111} grain boundary in an yttria-stabilized cubic zirconia bicrystal. Philos Mag Lett 82(7):393–400. https://doi.org/10.1080/09500830210137407

Shkurskiy BB (1998) About a possible relationship between the structure of twin boundaries and REE content in fluorite crystals. Proc of 18th European Cryst Meeting. Bull Czech and Slovak Crystallogr Assoc, Prague, p 199

Sobolev BP (2000) The Rare Earth Trifluorides: The high temperature chemistry of the rare earth trifluorides. Institut d'Estudis Catalans, Barcelona, Spain

Sobolev BP (2021) Nonstoichiometry in Inorganic Fluorides. IV: The Initial Stage of Anionic Nonstoichiometry in RF_3 (R=Y, La, Ln). Crystallogr Rep 66(3):349–360. https://doi.org/10.1134/S1063774521030238

Sobolev BP, Sorokin NI, Bolotina NB (2016) Nonstoichiometric Single Crystals $M_{1-x}R_xF_{2+x}$ and R_1–MF_3– (M = Ca, Sr, Ba: R= Rare Earth Elements) as Fluorine-Ionic Conductive Solid Electrolytes. Photonic and Electronic Properties of Fluoride Materials. Elsevier, pp 465–491. https://doi.org/10.1016/B978-0-12-801639-8.00021-0

Sulyanova EA, Sobolev BP (2022) The universal defect cluster architecture of fluorite-type nanostructured crystals. CrystEngComm 24(20):3762–3769. https://doi.org/10.1039/D2CE00280A

Symington AR, Molinari M, Brincat NA, Williams NR, Parker SC (2019) Defect segregation facilitates oxygen transport at fluorite UO_2 grain boundaries. Philos Trans R Soc A 377(2152):20190026. https://doi.org/10.1098/rsta.2019.0026

Urusov VS, Tauson VL, Akimov VV (1997) Solid state geochemistry. GEOS, Moscow

Vasilkova NN, Kukushkina ON (1989) Fluorite. Typomorphism of minerals. Guide. Nedra, Moscow, pp 492–501

Warrington DH (1974) Special grain boundaries in random polycrystalline aggregates. J Microsc 102(3):301–308. https://doi.org/10.1111/j.1365-2818.1974.tb04641.x

Wen C, Lanza M (2021) Calcium fluoride as high-k dielectric for 2D electronics. Appl Phys Rev 8(2):021314. https://doi.org/10.1063/5.0036987

Wood BJ, Fraser DG (1977) Elementary thermodynamics for geologists. Oxford University Press, Oxford

Zhang J et al (2023) Defect induced luminescence from surface modified calcium fluoride nanoparticles for in-situ temperature monitoring of lubricating oil. Appl Nanosci 13(1):275–282. https://doi.org/10.1007/s13204-020-01654-x

Zhu Q et al (2013) Evolutionary method for predicting surface reconstructions with variable stoichiometry. Phys Rev B 87(19):195317. https://doi.org/10.1103/PhysRevB.87.195317